



The First Interferometric Measurements of NH_2/NH_3 Ratio in Hot Corinos

Downloaded from: <https://research.chalmers.se>, 2025-12-05 03:12 UTC

Citation for the original published paper (version of record):

Yamato, Y., Furuya, K., Aikawa, Y. et al (2022). The First Interferometric Measurements of NH_2/NH_3 Ratio in Hot Corinos. *Astrophysical Journal*, 941(1).
<http://dx.doi.org/10.3847/1538-4357/ac9ea5>

N.B. When citing this work, cite the original published paper.



The First Interferometric Measurements of $\text{NH}_2\text{D}/\text{NH}_3$ Ratio in Hot Corinos

Yoshihide Yamato¹ , Kenji Furuya² , Yuri Aikawa¹ , Magnus V. Persson³ , John J. Tobin⁴ , Jes K. Jørgensen⁵ , and Mihkel Kama^{6,7}

¹ Department of Astronomy, Graduate School of Science, The University of Tokyo, 7-3-1 Hongo, Bunkyo-ku, Tokyo 113-0033, Japan;
yamato@astron.s.u-tokyo.ac.jp

² National Astronomical Observatory of Japan, Osawa 2-21-1, Mitaka, Tokyo 181-8588, Japan

³ Department of Space, Earth and Environment, Chalmers University of Technology, Onsala Space Observatory, SE-43992 Onsala, Sweden

⁴ National Radio Astronomy Observatory, 520 Edgemont Rd., Charlottesville, VA 22093, USA

⁵ Niels Bohr Institute, University of Copenhagen, Øster Voldgade 5–7, DK-1350 Copenhagen K., Denmark

⁶ Department of Physics and Astronomy, University College London, Gower Street, WC1E 6BT, London, UK

⁷ Tartu Observatory, University of Tartu, 61602 Tõravere, Tartumaa, Estonia

Received 2022 May 23; revised 2022 October 19; accepted 2022 October 28; published 2022 December 13

Abstract

The chemical evolution of nitrogen during star and planet formation is still not fully understood. Ammonia (NH_3) is a key specie in the understanding of the molecular evolution in star-forming clouds and nitrogen isotope fractionation. In this paper, we present high-spatial-resolution observations of multiple emission lines of NH_3 toward the protobinary system NGC1333 IRAS4A with the Karl G. Jansky Very Large Array. We spatially resolved the binary (hereafter, 4A1 and 4A2) and detected compact emission of NH_3 transitions with high excitation energies ($\gtrsim 100$ K) from the vicinity of the protostars, indicating the NH_3 ice has sublimated at the inner hot region. The NH_3 column density is estimated to be $\sim 10^{17}\text{--}10^{18}\text{ cm}^{-2}$. We also detected two NH_2D transitions, allowing us to constrain the deuterium fractionation of ammonia. The $\text{NH}_2\text{D}/\text{NH}_3$ ratios are as high as $\sim 0.3\text{--}1$ in both 4A1 and 4A2. From comparisons with the astrochemical models in the literature, the high $\text{NH}_2\text{D}/\text{NH}_3$ ratios suggest that the formation of NH_3 ices mainly started in the prestellar phase after the formation of bulk water ice finished, and that the primary nitrogen reservoir in the star-forming cloud could be atomic nitrogen (or N atoms) rather than nitrogen-bearing species such as N_2 and NH_3 . The implications on the physical properties of IRAS4A's cores are discussed as well.

Unified Astronomy Thesaurus concepts: [Astrochemistry \(75\)](#); [Star formation \(1569\)](#)

1. Introduction

Nitrogen is the fifth most abundant element in the interstellar medium (ISM) with an abundance of $\sim 6 \times 10^{-5}$ with respect to hydrogen (Przybilla et al. 2008). Determining the main nitrogen reservoirs in molecular clouds is a fundamental problem in astrochemistry. The nitrogen budget in molecular clouds also affects the formation of nitrogen-bearing complex organics molecules and chemistry in planet-forming disks (e.g., Schwarz & Bergin 2014).

In molecular clouds, the main nitrogen reservoirs in the gas phase are expected to be molecular nitrogen (N_2), which are formed in the gas phase (e.g., Furuya et al. 2018; van Dishoeck et al. 1993; see also Öberg & Bergin 2021). While in the central region of the clouds N_2 is self-shielded against interstellar UV photons and thus abundant, a substantial amount of atomic nitrogen (or N atoms) could also be present in the outer regions where the density is relatively low. N and N_2 freeze-out onto the surface of dust grains in the molecular clouds, and subsequently form other nitrogen-bearing molecules such as ammonia (NH_3) via a sequence of hydrogenation (Fedoseev et al. 2015; Hidaka et al. 2011; Jonusas et al. 2020). Nitrogen-bearing molecules are also formed via gas-phase reactions (e.g., Le Gal et al. 2014), and can successively deplete onto dust grain mantles (e.g., Caselli et al. 2022; Pineda et al. 2022).

However, the partition of elemental nitrogen into these species is still not well constrained (Öberg & Bergin 2021).

Observationally constraining the main nitrogen reservoirs is generally difficult. Neither N_2 nor atomic N in the gas phase can be observed due to the lack of low-energy transitions that can be excited at the low temperature in molecular clouds. Instead, Maret et al. (2006) used the N_2H^+ emission line in molecular cloud cores to constrain the N_2 abundance in the gas phase. N_2H^+ is primarily formed by $\text{N}_2 + \text{H}_3^+$, and thus its abundance reflects the abundance of gaseous N_2 . Based on the relatively weak N_2H^+ emission, they suggested that N_2 is not the main nitrogen reservoir, and instead atomic N in the gas phase would be. This is also consistent with the low N_2 abundance in comets. Rubin et al. (2015) made an in situ measurement of N_2 in the comet 67P/Churyumov–Gerasimenko, revealing that the N_2/CO ratio is depleted by a factor of ~ 25 compared with the case where all protosolar carbon and nitrogen are in CO and N_2 . Icy nitrogen-bearing species in molecular clouds have been observed in the infrared. While NH_3 ice absorption bands in the $3\text{ }\mu\text{m}$ band have long been debated, its $9.1\text{ }\mu\text{m}$ band has been clearly detected by (Lacy et al. 1998; see also Gibb et al. 2000). Observations with the Spitzer Space Telescope revealed that $\sim 10\%$ of overall nitrogen is locked up in ices, mainly as NH_3 (e.g., Öberg et al. 2011; Bottinelli et al. 2010; see also Boogert et al. 2015). Still, these relatively low NH_3 abundances imply that N_2 and N can be the main nitrogen reservoir in molecular clouds. Alternatively, there are also possibilities that a substantial amount of NH_3 is converted into ammonium salts, and that they can constitute a significant portion of the nitrogen reservoir as



Original content from this work may be used under the terms of the [Creative Commons Attribution 4.0 licence](#). Any further distribution of this work must maintain attribution to the author(s) and the title of the work, journal citation and DOI.

Table 1
Observed Transitions and Their Spectroscopic Data

Specie	Transition	ν_0 (GHz)	$\log_{10} A_{ul}$ (s ⁻¹)	g_u	E_u (K)
NH ₃	(1,1)	23.6944955	-6.78260	6.0	23.26484
	(2,2)	23.7226333	-6.65631	10.0	64.44806
	(3,3)	23.8701292	-6.59744	28.0	123.53904
	(4,4)	24.1394163	-6.55545	18.0	200.52091
	(5,5)	24.5329887	-6.51738	22.0	295.37076
NH ₂ D	3 _{1,3} -3 _{0,3}	18.807888	-7.42815	63.0	93.91931
	4 _{1,4} -4 _{0,4}	25.023792	-7.01363	27.0	152.25741

Notes. The spectroscopic data are retrieved from the Jet Propulsion Laboratory (JPL) Catalogue (Pickett et al. 1998) and Cologne Database for Molecular Spectroscopy (CDMS; Müller et al. 2005) via the Splatalogue interface. The original data are presented in Yu et al. (2010) for NH₃ and De Lucia & Helminger (1975), Cohen & Pickett (1982), and Fusina et al. (1988) for NH₂D.

observed in the comet 67P (Altwegg et al. 2020). In summary, observational constraints on the main nitrogen reservoir in molecular clouds and how they vary with the evolution from clouds to comets are still lacking.

The molecular D/H ratios of ice can probe the formation history of molecules. As deuterium fractionation is more efficient in dense, cold environments (e.g., molecular cloud cores; Millar et al. 1989), information about the formation stage of molecules is imprinted into molecular D/H ratios. Recently, Furuya & Persson (2018) proposed a new approach to constrain the main nitrogen reservoir in molecular clouds using the D/H ratios of NH₃ ice, i.e., NH₂D/NH₃.⁸ They performed gas-ice astrochemical simulations to investigate the evolution of nitrogen-bearing species from the formation of molecular clouds, a dense prestellar core, and then to the protostellar stage. They showed that if most nitrogen is already locked up in NH₃ ice in the molecular cloud stage, the NH₂D/NH₃ in bulk ice mantle, and thus the ratio in the sublimates in the central warm regions of protostellar envelopes (typically $\lesssim 100$ au and $\gtrsim 100$ K; so-called “hot corinos”), are as low as $\sim 4 \times 10^{-3}$, similar to or slightly higher than the HDO/H₂O ratio. If N atoms are the dominant nitrogen reservoir in molecular clouds and NH₃ ice formation commences only in the prestellar stage, on the other hand, the NH₂D/NH₃ ratio in the protostellar stage could be a few percent or even higher (e.g., Aikawa et al. 2012; Furuya & Persson 2018). The NH₂D/NH₃ ratio in the hot corinos, where ices sublimate, tells us when the NH₃ ice is mainly formed.

The deuteration of NH₃ in the cold outer envelopes of Class 0 protostars has been measured by single-dish observations. NH₂D/NH₃ ratios in the gas phase have been derived to be as high as a few to a few tens of percent (e.g., Hatchell 2003; Shah & Wootten 2001). Even doubly- and triply-deuterated ammonia (NHD₂ and ND₃) have been detected (e.g., Loinard et al. 2001; van der Tak et al. 2002). On the other hand, deuteration of NH₃ in a hot corino has not been measured so far, as high-resolution and high-sensitivity observations by interferometers are needed.

⁸ Strictly speaking, the D/H ratio of NH₃ is 1/3 of NH₂D/NH₃, since the chance for ammonia during its formation to have D is three times higher than, for example, C₂H. However, we use the term D/H ratio for the ratio of monodeuterated to normal isotopologues in the text for brevity. We consider this statistical issue when we compare the D/H ratio among molecules in Section 5.3.

One of the few sources where NH₃ emission has been detected in the hot corino is NGC1333 IRAS4A (hereafter IRAS4A), a deeply embedded low-mass Class 0 protobinary system located at a distance of ~ 300 pc (Ortiz-León et al. 2018; Zucker et al. 2020). IRAS4A harbors two protostars, IRAS4A1 and IRAS4A2 (hereafter 4A1 and 4A2; Lay et al. 1995; Looney et al. 2000). The $(J, K) = (2, 2)$ and $(3, 3)$ inversion transitions of NH₃ at 24 GHz have been observed by the Karl G. Jansky Very Large Array (VLA) toward 4A1 and 4A2 by Choi et al. (2007, 2010, 2011). Both 4A1 and 4A2 show compact emission of those transitions, indicative of the NH₃ ice sublimation. Most recently, De Simone et al. (2022) also observed $(J, K) = (3, 3)$ to $(7, 7)$ inversion transitions of NH₃ with the VLA, revealing abundant warm NH₃ gas sublimated from ice in the hot corino.

In this paper, we report the first detection of singly-deuterated ammonia (NH₂D) emission in the hot corinos of 4A1 and 4A2, using interferometric observations at centimeter wavelengths with the VLA. In Section 2, our observations and data reduction are described. We analyzed the NH₃ and NH₂D emission line profiles to constrain the NH₂D/NH₃ ratios in the central region of 4A1 and 4A2, as described in Section 3. In Section 4, constraints on the column densities of NH₃ and NH₂D, excitation temperatures, and NH₂D/NH₃ ratios are shown. We discuss the implications from the derived NH₂D/NH₃ ratios and constraints on the formation stage of NH₃ molecules in Section 5. Finally, we summarize our results in Section 6.

2. Observation

The IRAS4A system was observed with VLA during Semester 2018B (PI: Magnus V. Persson; project code: 18B-125). Two tracks of observations were performed in the C-configuration using its K-band receivers (18–26.5 GHz) on 2018 November 26 and 2019 January 19, both centered on 4A2 ($\alpha(J2000) = 03^{\text{h}}29^{\text{m}}10^{\text{s}}.440$, $\delta(J2000) = +031^{\circ}13'32''.160$). The phase, flux, and bandpass calibrators are J0336+3218, 0542+498 (3C147), and J3019+4130, respectively. The absolute flux calibration uncertainty for the K band is 10–15%.⁹

The observed data were split into 23 spectral windows, 10 of which were dedicated to continuum observations and 13 of which were used to observe the line emission. The spectral resolution and bandwidth of the line spectral windows are 7.812 kHz (~ 0.1 km s⁻¹) and 4 MHz (~ 50 km s⁻¹), respectively. The spectral setup targeted several NH₃ and NH₂D transitions, listed in Table 1, using seven out of 13 line spectral windows. Other spectral windows targeted ¹⁵NH₃ transitions and H₂O maser emission, which are not presented in this paper. We note that our correlator setup covers all the hyperfine satellites for the NH₃ (1,1) transition, while only the inner satellites are covered for the NH₃ (3,3) and NH₂D 3_{1,3}-3_{0,3} and 4_{1,4}-4_{0,4} transitions. For the NH₃ (4,4) and (5,5) transitions, the correlator setup does not cover the hyperfine satellites and only main lines are covered.

The data were calibrated using the VLA pipeline in Common Astronomy Software Applications (CASA) v5.4.1 (McMullin et al. 2007). Bad data were identified from an initial pipeline run. These data were flagged and the pipeline was rerun. To protect the spectral lines from radio frequency interference

⁹ <https://science.nrao.edu/facilities/vla/docs/manuals/oss/performance/fdscale>

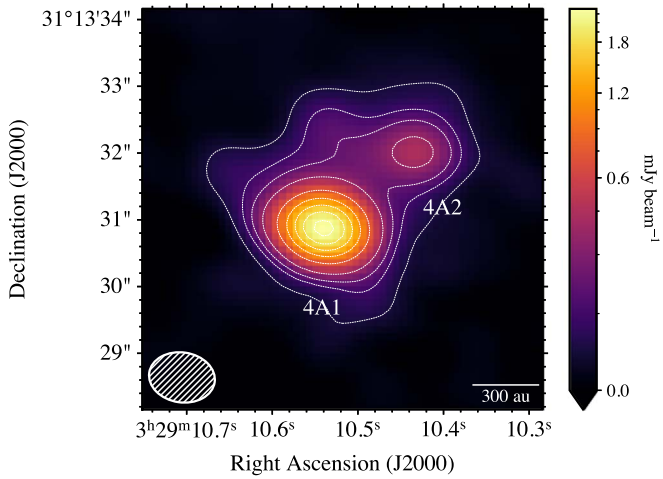


Figure 1. The 22.3 GHz continuum emission maps toward IRAS 4A1 and IRAS 4A2. The contours (white dashed lines) correspond to $[10, 20, 30, 50, 100, 150, 200, 250, 300] \times \sigma_{\text{RMS}}$, where $\sigma_{\text{RMS}} = 7.4 \mu\text{Jy beam}^{-1}$. The beam sizes of $0''.99 \times 0''.75$ (P.A. = 82°) and scale bars of 300 au are shown at lower left and right. We note that the color scales employ arcsinh stretches, with the lower end saturating at 0.0.

flagging and downweighting, we manually specified continuum regions in a `cont.dat` file for the spectral line windows. In order to identify the line-free channels in the spectral windows with many lines (e.g., NH_3 (1,1) hyperfines), we first Fourier transformed the visibilities of line spectral windows without any continuum subtraction. The line-free channels are manually selected by carefully inspecting the image cubes. Afterwards, continuum subtraction is done in the u - v plane using `uvcontsub` task for all line spectral windows specifying the line-free channels selected in the image plane.

The visibilities in all continuum spectral windows and line-free channels in line spectral windows are averaged to ~ 4 MHz channel widths, and deconvolved down to a $3 \times$ rms noise level of the dirty image using the multiscale CLEAN algorithm implemented in the `tclean` task with scales of $[0, 10, 30]$ pixels (with a pixel scale of $0''.1$) and a Briggs parameter of 0.5. To determine the CLEAN components, we used the *automasking* feature implemented in the `tclean` task with the parameters `sidelobethreshold` = 2.0, `noisethreshold` = 4.25, and `lownoisethreshold` = 1.5. We manually checked that all the emission components were masked by carefully inspecting the resulting image.

Figure 1 presents the 22.3 GHz (~ 1.3 cm) continuum image. The resulting beam size and rms noise level of the continuum image were $0''.99 \times 0''.75$ (P.A. = 82°) and $7.4 \mu\text{Jy beam}^{-1}$, respectively. The rms noise level was measured in the emission-free region. The continuum peak positions are estimated by the two-dimensional (2D) Gaussian fitting to be $\alpha(\text{J2000}) = 03^{\text{h}}29^{\text{m}}10^{\text{s}}540$, $\delta(\text{J2000}) = +031^\circ13'30''893$ for 4A1 and $\alpha(\text{J2000}) = 03^{\text{h}}29^{\text{m}}10^{\text{s}}442$, $\delta(\text{J2000}) = +031^\circ13'32''011$ for 4A2, which are consistent with those derived by De Simone et al. (2020). The peak intensities were $2.2 \pm 0.3 \text{ mJy beam}^{-1}$ and $0.42 \pm 0.06 \text{ mJy beam}^{-1}$ for 4A1 and 4A2, respectively. The flux calibration uncertainty was added in quadrature. These values are consistent with those derived by De Simone et al. (2020) within uncertainty.

The visibilities in line spectral windows are imaged using the multiscale CLEAN algorithm with scales of $[0, 10, 30]$ pixels, a Briggs parameter of 2.0, 1.0 km s^{-1} velocity channel widths, and the same *automasking* parameters as the continuum imaging. The properties of the images, such as beam sizes and rms noise levels (σ_{RMS}), are listed in Table 2.

Figure 2 shows a gallery of velocity-integrated emission maps for all NH_3 and NH_2D lines, generated using *better-moments* (Teague & Foreman-Mackey 2018). The image cubes are integrated over the velocity ranges listed in Table 2 encompassing all detected hyperfine components. The velocity ranges for integration are adjusted for each transition to include only the emission by visually inspecting the image cubes. The noise levels σ for these maps are calculated by *better-moments* as $\sigma = \sigma_{\text{RMS}} \times \sqrt{N} \times dv$, where N is the number of integrated channels and dv is the channel width (1.0 km s^{-1}). These values are reported in each panel of Figure 2. We clearly see the detection of all NH_3 lines toward both 4A1 and 4A2 at signal-to-noise ratios (S/Ns) of ~ 10 – 20 , while NH_2D lines are detected toward 4A1 with S/Ns of ~ 5 and only tentatively detected toward 4A2 with S/Ns of ~ 3 – 5 . These S/N values are reported in Table 2 as well.

3. Analysis

In order to estimate the column densities of NH_3 and NH_2D , first we extracted the spectra for all lines from a single pixel toward the continuum peak position estimated in Section 2 for each source. The extracted spectra are presented in Figures 3 and 4 for 4A1 and 4A2. For the following analysis, NH_3 (1,1) and (2,2) transitions are excluded: given their relatively low

Table 2
Properties of Image Cubes and Velocity-integrated Intensity Maps of NH_3 and NH_2D

Specie	Transition	rms (mJy beam^{-1})	Synthesized Beam (P.A.)	Integration Range ^a (km s^{-1})	S/N ^b	
					4A1	4A2
NH_3	(1, 1)	0.69	$1''.35 \times 0''.99(75^\circ)$	$[-14, -11], [-3, 1], [4, 9], [12, 16], [23, 29]$	12	16
NH_3	(2, 2)	0.62	$1''.32 \times 0''.98(75^\circ)$	$[-13, -8], [4, 10], [21, 26]$	9.2	13
NH_3	(3, 3)	0.60	$1''.31 \times 0''.98(75^\circ)$	$[-16, -11], [3, 11], [25, 30]$	10	18
NH_3	(4, 4)	0.55	$1''.25 \times 0''.95(77^\circ)$	$[3, 10]$	11	13
NH_3	(5, 5)	0.60	$1''.27 \times 1''.02(73^\circ)$	$[3, 10]$	9.0	14
NH_2D	$3_{1,3}-3_{0,3}$	0.59	$1''.52 \times 1''.23(81^\circ)$	$[4, 10]$	5.5	3.1
NH_2D	$4_{1,4}-4_{0,4}$	0.58	$1''.26 \times 0''.92(74^\circ)$	$[4, 10]$	5.2	4.9

Notes.

^a Integration ranges for velocity-integrated emission maps.

^b Peak signal-to-noise ratios on the velocity-integrated emission maps.

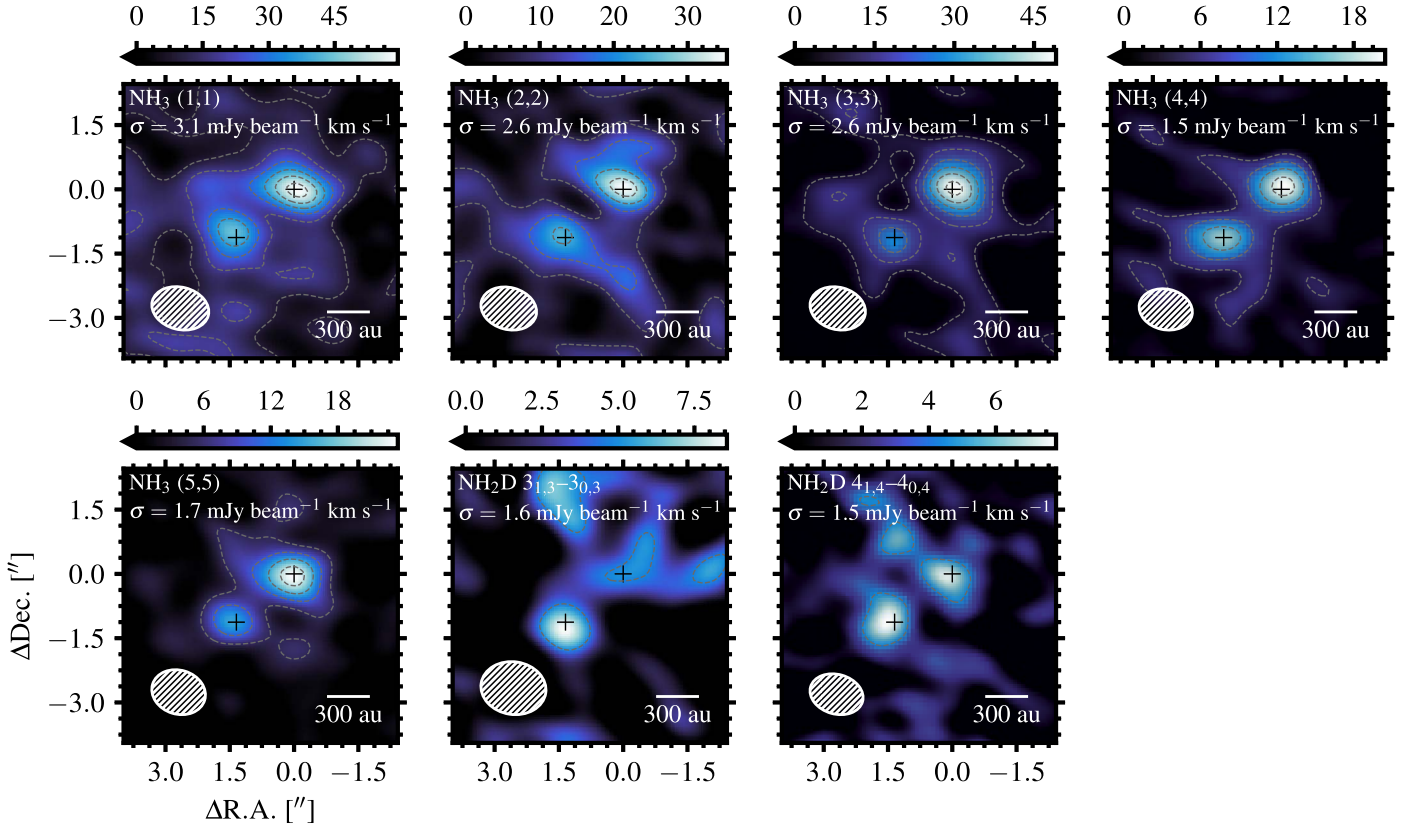


Figure 2. Gallery of velocity-integrated intensity maps of NH_3 and NH_2D transitions. Transitions are indicated at the upper left in each panel. The continuum emission peaks for 4A1 and 4A2 are indicated by black crosses in each panel. The gray dashed contours start from 3σ , followed by steps of 3σ . The beam size and scale bar of 300 au are shown in lower right and left in each panel, respectively. We note that the color scale is saturated at the lower end of 0.0.

IRAS 4A1

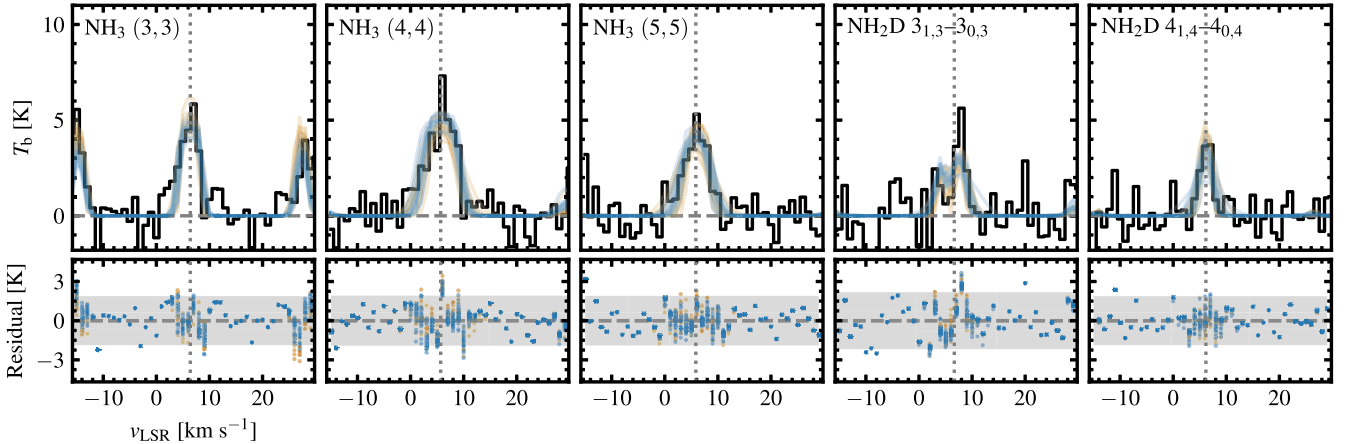


Figure 3. Top: observed spectra of NH_3 (3,3), NH_3 (4,4), NH_3 (5,5), NH_2D $3_{1,3}-3_{0,3}$, and NH_2D $4_{1,4}-4_{0,4}$ in brightness temperature (T_B) (black) extracted toward the continuum peaks of 4A1. The model spectra generated by 20 randomly selected parameter samples from the Markov Chain Monte Carlo (MCMC) chains of the fits with fixed (blue) and free (orange) ortho-to-para ratios of NH_3 are overlaid. Bottom: residual of observations and fitted model with fixed (blue) and free (orange) ortho-to-para ratio of NH_3 . Each data point corresponds to the randomly selected models from MCMC chains. The gray-shaded regions indicate the $2\sigma_{\text{RMS}}$ range. For both the top and bottom panels, while the zero flux levels are indicated by gray dashed horizontal lines, the vertical dotted lines indicate the systemic velocity.

excitation energies, the extended emission may contaminate the emission from the central hot region.

3.1. Estimates on the Emitting Region Size

To estimate the emitting region size, we inspected the visibility profiles in the (u,v) plane (amplitude–baseline length plot) for each transition. However, all of the transitions show

almost flat profiles, indicating that it is difficult to infer the emitting region size even from visibility data. Instead, we estimated the emitting region size of NH_3 using our data and the data presented in Choi et al. (2010, 2011). Choi et al. (2010, 2011) observed NH_3 (3,3) transitions toward the IRAS4A system with a circular beam of $0''.3 \times 0''.3$, which is a higher spatial resolution than our data. The difference in the beam sizes between the data in Choi et al. (2010, 2011) and our

IRAS 4A2

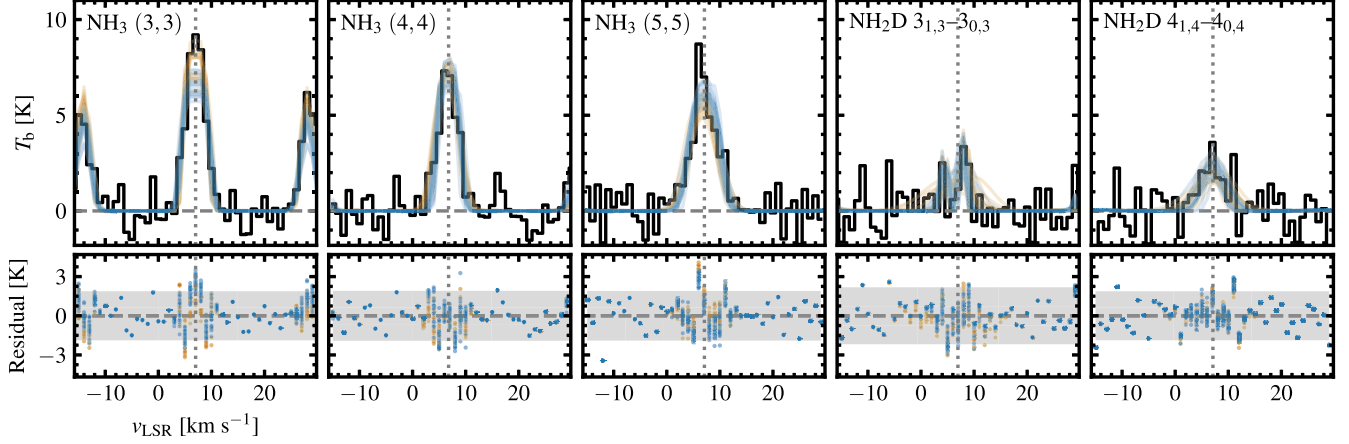


Figure 4. Same as Figure 3, but for 4A2.

data allows us to evaluate the beam dilution and accurately estimate the emitting region size, assuming that both observations trace the region with the same physical condition and that the lines are optically thick. We will confirm that the main component of NH_3 (3,3) is highly optically thick ($\tau \gtrsim 10$) in the following section.

We fitted a Gaussian to the spectra presented in Figure 4 in Choi et al. (2011) and Figure 1 in Choi et al. (2010) for IRAS4A1 and IRAS4A2, resulting in peak brightness temperatures of 44.4 ± 2.3 K and 73.2 ± 2.5 K, respectively. We also fitted a Gaussian to the NH_3 (3,3) main component of our data to obtain the peak brightness temperature. The observed peak brightness temperatures can be modeled as $T_{\text{int}} \times f$, where T_{int} is the intrinsic temperature and f is the beam filling factor, given as

$$f = \frac{\theta_s}{\sqrt{\theta_s^2 + \theta_{\text{maj}}^2}} \frac{\theta_s}{\sqrt{\theta_s^2 + \theta_{\text{min}}^2}}, \quad (1)$$

where θ_s is the emitting region size and θ_{maj} and θ_{min} are the size of the beam major and minor axes, respectively. Here we assume that the emission distribution of the source is a symmetric 2D Gaussian with a FWHM of θ_s . Assuming that T_{int} is the same between the data, the relation between the observed peak brightness temperature ratio and θ_s can be inferred. We constructed the likelihood function of the observed brightness temperature ratio and θ_s . To sample the posterior distribution, we employed a Markov Chain Monte Carlo (MCMC) method implemented in the `emcee` python package (Foreman-Mackey et al. 2013). We used a uniform prior in the interval $[0''.01, 0''.6]$ for θ_s and ran 200 walkers for 600 steps, including an initial 100 steps discarded as burn-in. We found $\theta_s = 0''.25^{+0.05}_{-0.06}$ and $0''.30^{+0.03}_{-0.03}$ for 4A1 and 4A2, respectively, where the estimated values are the median of the posterior distributions and uncertainties are the 16th and 84th percentile. These estimates are used in the subsequent analyses. The estimated emitting region is close to the beam size of Choi et al. (2010), in which the deconvolved sizes of the sources are derived to be $0''.44 \times 0''.25$ for 4A1 and $0''.55 \times 0''.30$ for 4A2. These values are slightly larger than our estimates, most probably because they averaged the images of (2,2) and (3,3), while our estimates are based on the (3,3) transition only.

3.2. Hyperfine Fit of NH_3 and NH_2D Lines

We fitted the observed spectra with a synthetic model considering hyperfine splitting (Rosolowsky et al. 2008). The details of the model used in the present work are described in Appendix A. Among the observed NH_3 and NH_2D transitions, both ortho (NH_3 (3,3) and NH_2D (3,3)) and para (NH_3 (4,4), (5,5), and NH_2D (4,4)) transitions are included, which in principle allows us to estimate the ortho-to-para ratio of NH_3 and NH_2D . In our model, we assume local thermodynamical equilibrium (LTE) so that the observed spectra can be fitted by a common excitation temperature for NH_3 and NH_2D transitions under the assumption that they originate from the same gas. The LTE assumption should be valid for targeted sources because the H_2 density in the vicinity of the protostar ($\lesssim 100$ au) should be $\gtrsim 10^6 \text{ cm}^{-3}$ (e.g., De Simone et al. 2020; Persson et al. 2016), which is far higher than the critical densities of NH_3 transitions ($\sim 10^3 \text{ cm}^{-3}$; e.g., Shirley 2015).

First, we fitted these models to the NH_3 and NH_2D line profiles simultaneously; the ortho-to-para ratios of NH_3 and NH_2D are fixed to 1 and 3, respectively, which are the statistical values expected in the warm ($\gtrsim 100$ K) environments. This resulted in 14 free parameters (Table 3): velocity dispersions (ΔV) and systemic velocities (v_{sys}) for all five transitions, the logarithms of column densities of NH_3 and NH_2D ($\log_{10} N(\text{NH}_3)$ and $\log_{10} N(\text{NH}_2\text{D})$), and the common excitation temperature (T_{ex}) and emitting region size (θ_s) among all five transitions. We also ran a fit with the ortho-to-para ratio of NH_3 as a free parameter to check if the assumption of statistical equilibrium affects the derived parameters. We sampled the posterior distributions with a MCMC method implemented in the `emcee` Python package. We used uniform priors for all parameters except for the emitting region size. We used tight Gaussian priors for emitting region sizes based on the estimates in previous subsections. We ran 200 walkers for 5000 steps, including an initial 2500 steps discarded as burn-in. During the fit, we initially generated model spectra with much higher velocity samplings and then resampled down to the ones in the actual data (1.0 km s^{-1}).

4. Results

The observed spectra overlaid by the model spectra generated from posterior samples, as well as the residual

Table 3
Free Parameters of Hyperfine Fits for 4A1 and 4A2

Parameter	Prior for 4A1 Fit ^a	Prior for 4A2 Fit ^a
ΔV (km s ⁻¹) ^b	U [0.1, 10]	U [0.1, 10]
v_{sys} (km s ⁻¹) ^c	U [4, 10]	U [4, 10]
$\log_{10} N(\text{NH}_3)$ (cm ⁻²)	U [14, 21]	U [14, 21]
$\log_{10} N(\text{NH}_2\text{D})$ (cm ⁻²)	U [14, 21]	U [14, 21]
T_{ex} (K)	U [50, 350]	U [50, 350]
θ_s (")	G [0.25, 0.06]	G [0.30, 0.03]
o/p ^c	U [0.01, 100]	U [0.01, 100]

Notes.

^a The prior distributions of the parameter. The type of prior (uniform or Gaussian) and its parameters are listed. “U” represents a uniform prior, followed by the lower and upper bound of the uniform prior. “G” represents a Gaussian prior, followed by the center and standard deviation of the Gaussian prior.

^b The priors are common for all transitions, while treated as individual parameters for each transition.

^c The ortho-to-para ratio of NH₃. Used for fits with free ortho-to-para ratio only.

spectra after subtracting the model spectra, are presented in Figures 3 and 4. The results of the fits are summarized in Table 4.

For 4A1, high excitation temperatures are derived in both fits with the ortho-to-para ratio fixed and varied (98^{+8}_{-7} K and 110^{+10}_{-10} K, respectively). The total optical depth (including the hyperfine) of each NH₃ transition is greater than unity, while the hyperfine satellites of the NH₃ (3,3) transition provide the constraints on the column density of NH₃. In the fits with free ortho-to-para ratio, the NH₃ column density is more uncertain and the NH₃ ortho-to-para ratio is not well constrained. Since a statistical NH₃ ortho-to-para ratio of unity is expected in the hot region, we employ the fit with the fixed ortho-to-para ratio as the fiducial result. The NH₂D column densities result in similar values ($\sim 7 \times 10^{17}$ cm⁻²) in both fits. Particularly, the undetected hyperfine satellites of NH₂D ($4_{1,4}-4_{0,4}$) at ~ -16 km s⁻¹ and ~ 26 km s⁻¹ (see Figure 3) are helpful to constrain the column density. The line widths of the NH₃ (4,4) and (5,5) transitions are broader than those of the NH₃ (3,3) and NH₂D transitions (Table 4). This may indicate that these higher transitions of NH₃ preferentially trace inner regions with a higher infall velocity than (3,3) transition of NH₃ and NH₂D transitions. We will discuss this issue in more detail in Section 5. Finally, both fits yield high NH₂D/NH₃ column density ratios of $0.96^{+0.76}_{-0.39}$ and $0.28^{+0.59}_{-0.23}$, consistent within the uncertainties.

For 4A2, the fit with a fixed ortho-to-para ratio yields a lower excitation temperature (87^{+13}_{-10} K) than that with a free ortho-to-para ratio (160^{+30}_{-20} K). In the former, the peak brightness temperature of the main component of the NH₃ (3,3) transition is significantly underestimated (Figure 4), and thus the lower excitation temperature is not reasonable. In contrast, the spectra are better reproduced in the fit with a free ortho-to-para ratio, which suggests that the higher excitation temperature is more reasonable. However, the obtained ortho-to-para ratio of NH₃ in the fit ($4.5^{+1.5}_{-1.3}$) is significantly higher than the statistical ratio of unity. This does not seem to be realistic since the ortho-to-para ratio of NH₃ should be unity in the hot region, as indicated by the derived excitation temperature. Nevertheless, the column density estimates in the two fits agreed within the

uncertainties. We thus adopt the NH₃ column density derived from the fits with free ortho-to-para ratio as our fiducial value. The NH₂D column density is also well constrained, although the line widths are not well constrained due to the lower S/N. The widths of NH₃ lines are typically $\sim 2-5$ km s⁻¹, and broader for higher excitation transitions (Table 4). This could again imply that the emitting region is smaller (i.e., inner region with higher velocity) for higher transitions. Finally, the fiducial fit yields a NH₂D/NH₃ ratio of $0.48^{+0.17}_{-0.13}$, consistent with that derived in the fit with fixed ortho-to-para ratio within the uncertainties.

5. Discussion

5.1. NH₃ and NH₂D in the Hot Corino Region

We have detected high-excitation transitions of NH₃ (4,4) and (5,5) toward both 4A1 and 4A2 in addition to the (2,2) and (3,3) lines which were previously detected by Choi et al. (2007, 2010). The excitation temperatures derived in the hyperfine fits (~ 100 K for 4A1 and ~ 150 K for 4A2) are comparable to or higher than the typical NH₃ sublimation temperature of 100–140 K, depending on the gas density and composition of ice mixture (Furuya & Aikawa 2014; Hama & Watanabe 2013; Minissale et al. 2022). Since the gas and dust temperatures are expected to be well coupled in the high-density region, the high excitation temperatures indicate that the observed emission traces the NH₃ ice sublimation zone in the vicinity of the protostars. This conclusion is also supported by the compact emitting regions ($\sim 0''.25$ or ~ 75 au) and the high column density of NH₃ ($\sim 10^{17}-10^{18}$ cm⁻²). Taquet et al. (2013) derived the column density of sublimated H₂O to be $(3-5) \times 10^{19}$ cm⁻² toward IRAS4A, assuming an emitting region size of $\sim 0''.4$. The NH₃/H₂O abundance ratio of $10^{-2}-10^{-1}$ is consistent with the composition of interstellar ices observed toward low-mass protostars (Öberg et al. 2011). In addition to NH₃, we have detected high-excitation transitions of NH₂D. The observed line profiles are reasonably reproduced by the same emitting region sizes and excitation temperature as those of NH₃, suggesting that the observed emission traces NH₂D sublimated from ices. The NH₂D column densities are also high, resulting in high NH₂D/NH₃ ratios of $\sim 0.5-1$ toward both 4A1 and 4A2.

The high NH₂D/NH₃ ratios, higher than expected from Furuya & Persson (2018), motivate careful discussions and confirmation. First, the NH₃ column densities may be underestimated, as the NH₃ lines are optically thick. In particular, our spectral windows do not cover the hyperfine satellites of the NH₃ (4,4) and (5,5) transitions that can be optically thin ($\tau < 1$). De Simone et al. (2022) observed higher excitation lines up to $(J, K) = (7, 7)$ covering all of the hyperfine satellites, which allowed them to accurately estimate the column density of NH₃ with non-LTE large velocity gradient analysis. While our estimates of the NH₃ column density in 4A2 ($\sim 1 \times 10^{18}$ cm⁻²) are consistent with the estimates by De Simone et al. (2022; $(0.6-3) \times 10^{18}$ cm⁻² with a best fit of 2×10^{18} cm⁻²), our estimate for 4A1 ($\sim 8 \times 10^{17}$ cm⁻²) is lower by a factor of a few than their estimates ($(1-5) \times 10^{18}$ cm⁻² with a best fit of 2×10^{18} cm⁻²). In their work, the optically thin (7,7) transition allowed them to constrain the column density. Our analysis may indeed underestimate the NH₃ column density, particularly in 4A1. It is also possible that the column density of para-NH₃ that was constrained from NH₃

Table 4
Results of Fits for 4A1 and 4A2

o/p ^a	θ_s ["]	T_{ex} (K)	ΔV_{FWHM} (km s ⁻¹)					$N(\text{NH}_3)$ (cm ⁻²)	$N(\text{NH}_2\text{D})$ (cm ⁻²)	$\text{NH}_2\text{D}/\text{NH}_3$	Fiducial
			NH ₃ (3,3)	NH ₃ (4,4)	NH ₃ (5,5)	NH ₂ D 3 _{1,3} -3 _{0,3}	NH ₂ D 4 _{1,4} -4 _{0,4}				
IRAS4A1											
1 (fixed)	0.25 ^{+0.06} _{-0.06}	98 ⁺⁸ ₋₇	1.9 ^{+0.3} _{-0.2}	3.9 ^{+0.7} _{-0.6}	3.5 ^{+0.9} _{-0.7}	1.8 ^{+0.8} _{-0.5}	1.6 ^{+1.1} _{-0.8}	8.1 ^{+4.0} _{-2.5} × 10 ¹⁷	7.3 ^{+5.4} _{-1.9} × 10 ¹⁷	0.96 ^{+0.76} _{-0.39}	✓
11 ⁺⁴⁰ ₋₈	0.25 ^{+0.06} _{-0.06}	110 ⁺¹⁰ ₋₁₀	1.3 ^{+0.3} _{-0.2}	4.7 ^{+1.0} _{-0.8}	4.3 ^{+1.0} _{-0.8}	1.9 ^{+0.8} _{-0.5}	1.6 ^{+1.1} _{-0.8}	2.8 ^{+11.0} _{-2.0} × 10 ¹⁸	6.9 ^{+3.8} _{-1.6} × 10 ¹⁷	0.28 ^{+0.59} _{-0.23}	
IRAS4A2											
1 (fixed)	0.33 ^{+0.02} _{-0.03}	87 ⁺¹³ ₋₁₀	2.2 ^{+0.2} _{-0.2}	2.2 ^{+0.3} _{-0.2}	4.1 ^{+0.7} _{-0.7}	0.9 ^{+2.0} _{-0.5}	5.1 ^{+2.0} _{-1.6}	7.9 ^{+2.5} _{-1.6} × 10 ¹⁷	3.1 ^{+1.2} _{-1.0} × 10 ¹⁷	0.38 ^{+0.17} _{-0.13}	
4.5 ^{+1.5} _{-1.3}	0.26 ^{+0.02} _{-0.02}	160 ⁺³⁰ ₋₂₀	2.0 ^{+0.2} _{-0.2}	3.0 ^{+0.6} _{-0.5}	4.7 ^{+0.6} _{-0.6}	2.0 ^{+5.2} _{-1.3}	5.1 ^{+2.0} _{-1.5}	1.0 ^{+0.3} _{-0.2} × 10 ¹⁸	4.9 ^{+1.9} _{-1.4} × 10 ¹⁷	0.48 ^{+0.17} _{-0.13}	✓

Note.
^a The ortho-to-para ratio of NH₃.

(4,4) and (5,5) is underestimated due to the lack of hyperfines; this might cause the peculiar ortho-to-para ratio in one of the fits. The $\text{NH}_2\text{D}/\text{NH}_3$ best-fit ratios are still higher than the model prediction, 0.4 for 4A1 and 0.3 for 4A2, if we adopt the best-fit NH_3 column densities derived by De Simone et al. (2022).

Another possible caveat is that the kinetic gas motion could deviate the line profile from a simple Gaussian, which also could alter the estimation of column density and $\text{NH}_2\text{D}/\text{NH}_3$ ratios. Gas infall motion of the envelope can result in a blue-skewed or inverse P-Cygni profile, which has already been observed toward the IRAS4A system (e.g., CH_3OH and H_2O lines; Di Francesco et al. 2001; Kristensen et al. 2012; Mottram et al. 2013; Sahu et al. 2019). Indeed, the observed spectra of NH_3 (3,3) and (4,4) toward 4A1 in Figure 3 show subtle deviations from a Gaussian with rapid intensity decreases at the redshifted wings, which may trace the infall motion of the envelope, although it could also be due to the noise. The disk rotation could affect the line profile as well. Keplerian rotation of the circumstellar disk with a significant inclination will result in a double-peaked profile. Although more sophisticated modeling that includes these physical structures is desirable to more accurately evaluate the deuteration of NH_3 , our results of high deuteration would not change qualitatively as no clear evidence of infall or rotation is detected at the current spatial/spectral resolution and sensitivity.

Finally, we note that the line widths are different among the observed transitions (Table 4). In particular, the line widths of NH_3 (4,4) and (5,5) are broad compared to the other transitions,¹⁰ which may indicate that these transitions trace the more inner regions where the gas infall velocities are larger. If freefall ($v \propto r^{-0.5}$) is assumed as the gas kinetics, the difference in line widths between NH_3 (4,4) and (5,5) ($\sim 4 \text{ km s}^{-1}$) and the other transitions ($\sim 2 \text{ km s}^{-1}$) indicates the 4 times smaller radius of the emitting region for the former. We thus conducted the fit described in Section 3 using only the NH_3 (3,3) and NH_2D transitions, all of which show a similar line width. Assuming an ortho-to-para ratio of NH_3 of unity, the column densities of NH_3 and NH_2D , and thus the $\text{NH}_2\text{D}/\text{NH}_3$ ratios, are consistent with those of fiducial fits in Table 4 within uncertainties. Therefore, the high $\text{NH}_2\text{D}/\text{NH}_3$ ratio should be trustworthy at the spatial scales traced by NH_3 (3,3) and NH_2D transitions (i.e., $\sim 0''.25$ or $\sim 75 \text{ au}$).

Yet it is possible that the distributions of NH_3 (traced by (4,4) and (5,5)) and NH_2D are different at smaller spatial scales. Namely, the narrower line widths of NH_2D may imply that the line emission originates from more outer regions than the (4,4) and (5,5) NH_3 lines, e.g., a ring-like distribution of NH_2D . The $\text{NH}_2\text{D}/\text{NH}_3$ ratio derived in $\sim 0''.25$ scale then would be a lower limit for the ring regions and upper limit for the inner region with higher velocity, while we need higher spatial and/or spectral resolution to confirm such radial distribution. The ring region of a very high $\text{NH}_2\text{D}/\text{NH}_3$ ratio could be due to sublimation of a multilayered ice mantle (see Section 5.2)

5.2. Comparison with Theoretical Models and Origin of High $\text{NH}_2\text{D}/\text{NH}_3$ Ratios

Shah & Wootten (2001) detected NH_2D rotation-inversion transitions at 86 GHz and 110 GHz with the NRAO 12 m telescope. They derived $\text{NH}_2\text{D}/\text{NH}_3$ ratios of ~ 0.07 at the $\sim 24,000 \text{ au}$ scale in the circumbinary envelope of the IRAS4A system. Hatchell (2003) also observed the 86 GHz transitions with the IRAM 30 m telescope to obtain an $\text{NH}_2\text{D}/\text{NH}_3$ ratio of ~ 0.25 at the $\sim 7000 \text{ au}$ scale. These values are consistent with predictions of theoretical models (e.g., Aikawa et al. 2012; Furuya & Persson 2018; Taquet et al. 2014). In those models, the molecular D/H ratios in the cold outer envelope (typically at radii outside a few hundreds of au) are controlled by the exothermic exchange reactions in the gas phase. For example, NH_3 can be formed from NH , which is a product of dissociative recombination of N_2H^+ ; NH reacts with H_3^+ to form NH_2^+ , which is converted to NH_4^+ via sequential reactions of H_2 . NH_3 is formed by the dissociative recombination of NH_4^+ . In dense cold regions, H_3^+ is highly deuterated due to the exchange reaction and CO depletion, and its high D/H ratio propagates to N_2H^+ and thus to NH_3 (e.g., Aikawa et al. 2005). If nitrogen atoms are abundant in the cold region, NH_3 can be formed more efficiently via hydrogenation of N atoms on grain surfaces than via gas-phase reactions. They are also deuterated by abundant deuterium atoms, which are formed by dissociative recombination of H_2D^+ . NH_3 and NH_2D formed on cold grain surfaces, however, remain in the ice phase, and desorb only inefficiently via nonthermal desorption at low temperatures (Martín-Doménech et al. 2014; Hama & Watanabe 2013; Tinacci et al. 2022).

In the central region (typically $\lesssim 100 \text{ au}$), on the other hand, the temperature increases to $\gtrsim 100 \text{ K}$. Volatiles such as NH_3 start to sublime from the grain surface and their gas-phase abundances rapidly increase. In this region, the molecular D/H ratios reflect those of sublimated ice (e.g., Furuya & Persson 2018). While the sublimated molecules are subject to gas-phase reactions, the typical destruction timescale via gas-phase reactions is $\sim \text{several } 10^4 \text{ yr}$ (e.g., Nomura & Millar 2004). Even if we consider the enhanced ionization by X-rays (Notsu et al. 2021), the infall timescale would be shorter than the chemical timescale in the compact hot corino region ($\lesssim 100 \text{ au}$). The high excitation temperature ($\gtrsim 100 \text{ K}$) and high column densities of NH_3 and NH_2D are indeed consistent with ice sublimation. The derived $\text{NH}_2\text{D}/\text{NH}_3$ ratios (~ 0.5 – 1 from our analysis, or ~ 0.3 – 0.4 adopting the NH_3 column density of De Simone et al. 2022) are, however, significantly higher than predicted in Furuya & Persson (2018), i.e., a few % even in their N-atom-rich model.

Since our $\text{NH}_2\text{D}/\text{NH}_3$ ratios are similar to the ratio obtained in the outer envelope (~ 0.25) by Hatchell (2003), one may wonder if our observations partially trace the emission of NH_2D from the cold- or intermediate-temperature regions. While the estimated emitting region sizes, which can be used as a proxy of the sublimation region of NH_3 , are $\sim 0''.25$ or $\sim 75 \text{ au}$, the spatial resolution of our observations are much lower, i.e., $\sim 1''$ or $\sim 300 \text{ au}$. In addition, even intermediate temperatures (e.g., $\sim 50 \text{ K}$) could excite observed NH_3 and NH_2D transitions with energy levels of 90–150 K from the ground state. We thus conducted a non-LTE radiative transfer simulation of a free-falling envelope model and compared the simulated spectra with the observed spectra (see Appendix B

¹⁰ Although $\text{NH}_2\text{D } 4_{1,4}-4_{0,4}$ toward 4A2 is also broad, we do not consider this as a robust result due to the relatively low S/N of the line.

Table 5
Molecular D/H Ratios Measured toward the Inner Warm Region of the IRAS4A2 Core and the Comet 67P/C-G

Source	HDO/H ₂ O	(CH ₂ DOH + CH ₃ OD)/CH ₃ OH	NH ₂ D/NH ₃	References
IRAS4A	$5.4 \pm 1.5 \times 10^{-4}$	$(1.5\text{--}4.7) \times 10^{-2}$	$4.8^{+1.7}_{-1.3} \times 10^{-1}$	1, 2, 3, 4
67P/C-G	$1.05 \pm 0.14 \times 10^{-3}$	$5.6 \pm 1.2 \times 10^{-2}$	$\sim 1 \times 10^{-3}$	5, 6, 7

Note. The values in IRAS4A2 are shown as representatives of the IRAS4A system.

References. (1) Persson et al. (2014); (2) Jensen et al. (2019); (3) Taquet et al. (2019); (4) this work; (5) Altwegg et al. (2017); (6) Drozdovskaya et al. (2021); (7) Altwegg et al. (2019).

for details). We confirmed that the observed NH₂D emission is dominated by the emission from the hot corinos.

The very high NH₂D/NH₃ ratio and the possible ring-like distribution of NH₂D could be due to a multilayered structure of the ice mantle. Taquet et al. (2014), who calculated gas-grain chemistry of a star-forming core as in Furuya & Persson (2018), explicitly showed the fractional abundances of icy molecules in each monolayer of ice mantle. While the NH₂D/NH₃ ratio is $\lesssim 10^{-2}$ in the deep layers that are formed in early times, the ratio is ~ 0.3 in the surface layers of ice when the dense prestellar core is about to collapse. As the ice-coated grains enter the central warm region of the core, the highly deuterated ice on the grain surface will be the first to sublimate.

Even though NH₂D may be distributed in a ring region, our observation suggests that N atoms are the major nitrogen reservoir in molecular clouds. The NH₃ column density estimated from the (3,3) transition, which has a similar line width as that of NH₂D, is similar to the column density derived from the combination with higher transitions (see Section 5.2). The ammonia formed in the cold prestellar stage with a high D/H ratio is thus at least comparable in amount to that in the innermost regions. Since icy ammonia is more efficiently formed via hydrogenation of N atoms on the grain surfaces than in the gas phase, atomic nitrogen should be abundant and remains as the main nitrogen reservoir in the prestellar core stage, where enhanced deuteration is possible. In the model of Taquet et al. (2014), which predicts relatively abundant NH₃ ice and very high NH₂D/NH₃ in the surface of ice mantle, the nitrogen is assumed to be all atomic in their initial condition.

Furuya & Persson (2018) showed that the [NHD₂/NH₂D]/[NH₂D/NH₃] ratio could better trace the primary nitrogen reservoir than the NH₂D/NH₃ ratio alone. If the atomic nitrogen is largely converted into molecular forms such as N₂ and NH₃ in the early stage of molecular clouds, most of the ammonia ices should have formed by then, which results in a relatively low NH₂D/NH₃ ratio. NHD₂ is yet formed mainly in the later prestellar stage, since it requires more deuterium atoms, and the NHD₂/NH₂D ratio will be higher than NH₂D/NH₃, i.e., [NHD₂/NH₂D]/[NH₂D/NH₃] > 1. On the other hand, if atomic nitrogen remains the dominant nitrogen reservoir in the prestellar phase, which is likely the case for IRAS4A, all the deuterated isotopologues will be formed in the prestellar phase, and [NHD₂/NH₂D]/[NH₂D/NH₃] will be the statistical ratio ($\sim 1/3$). Thus, observations of doubly-deuterated NH₃ emission are desirable to confirm our conclusion.

5.3. Comparison with Other Major Species in Hot Corinos and Comet 67P/Churyumov–Gerasimenko

The first measurement of the NH₂D/NH₃ ratios achieved in this work enables us to compare the molecular D/H ratios

among molecules in hot corinos. Comparison with cometary D/H ratios is also important, since the molecules in hot corinos could be incorporated to protoplanetary disks and then to planetary material. The D/H ratios of major species such as water and methanol in the inner warm regions of protostellar cores have extensively been studied with regard to several sources including IRAS4A (e.g., Jensen et al. 2019; Persson et al. 2014; Taquet et al. 2019). Recent in situ measurements on the comet 67P/Churyumov–Gerasimenko (hereafter 67P) by the Rosetta project (Altwegg et al. 2019) has revealed the molecular D/H ratios in major volatiles. The observed molecular D/H ratios toward IRAS4A and comet 67P are summarized in Table 5. We note that the D/H ratios of water and methanol toward IRAS4A are available only toward 4A2 because the deuterated as well as normal isotopologues have not been detected in emission toward 4A1 in (sub)millimeter wavelengths, probably due to absorption by the highly optically thick dust. We note that the following comparison stands even if we adopt the NH₃ column density derived in De Simone et al. (2022), which results in NH₂D/NH₃ ~ 0.3 .

Among water, methanol, and ammonia, water shows the lowest D/H ratios of $\sim 10^{-4}$ toward IRAS4A (Persson et al. 2014; see also Jensen et al. 2019). This has been interpreted as evidence that the water ices are mainly formed in the early molecular cloud phase (Furuya et al. 2016). We note that, in the comparison of the D/H ratios among molecules, we need to take into account the hydrogen number in the normal isotopologue; e.g., the chance for NH₃ to get one hydrogen replaced by deuterium is 3/2 times higher than for H₂O. The HDO/H₂O ratio is still significantly low compared with the deuteration fraction of CH₃OH and NH₃.

In contrast to water, methanol shows higher D/H ratios of $\sim 10^{-2}$ toward IRAS4A (Taquet et al. 2019), suggesting the formation of methanol ices in the cold prestellar core phase. Higher D/H ratios of methanol than water are also seen in other protostellar cores such as IRAS2A and IRAS 16293-2422 (Manigand et al. 2020; Persson et al. 2014; Jørgensen et al. 2018; Taquet et al. 2019). The D/H ratio of ammonia measured toward IRAS4A in this work ($\gtrsim 10^{-1}$) is higher than that of methanol. We note that the D/H ratio of NH₃ is still higher than that of methanol, even if we consider the statistical correction and uncertainties associated with the observations. The lower limit of the NH₂D/NH₃ ratio is ~ 0.3 in 4A2 if we consider the uncertainty discussed in Section 5.1. This is higher than the upper limit of the (CH₂DOH + CH₃OD)/CH₃OH ratio by a factor of ~ 6 (Table 5). With the statistical correction, the D/H ratio of NH₃ is higher than that of CH₃OH by a factor of ~ 9 . This indicates that the ammonia ices are mostly formed in the later stage of prestellar cores, possibly even later than the formation of methanol ices, where the deuteration is more efficient. Observations of ammonia deuteration toward other

hot corinos are desirable to confirm that the high D/H ratio and late formation of ammonia ices are general.

The D/H ratios of water and methanol in the comet 67P shows a similar trend to those in IRAS4A (i.e., water D/H is lower than methanol; Altwegg et al. 2017, 2019; Drozdovskaya et al. 2019), suggesting the inheritance of the volatiles in the star-forming core to the planetary materials. The correlation in COMs abundances between the hot corinos and the comets also supports such an inheritance (Bianchi et al. 2019; Drozdovskaya et al. 2019). On the other hand, the D/H ratio of ammonia in the comet 67P is lower than methanol, which is different from the relation in IRAS4A. It suggests some chemical reprocessing for ammonia ices, or nitrogen as a whole, during the accretion onto the protostellar disk or subsequent protoplanetary disk stage. In the coma of comet 67P, Altwegg et al. (2020) recently detected a substantial amount of ammonium salts, which implies the chemical processes of ammonia. Alternatively, 67P inherits the low D/H component of ammonia, which is probed as a high-velocity component in our observation, while the high D/H component is fully released to the gas phase as discussed in Section 5.1. Indeed, Furuya et al. (2017) showed that stellar UV radiation can selectively remove the high D/H component from the surface of the ice via photodesorption, and the D/H ratios of water can be lower in the protoplanetary disk than those in protostellar envelopes. The same mechanism may work for ammonia as well.

5.4. Physical Properties of 4A1 and 4A2 Cores Probed by NH_3 and NH_2D

Although detailed modeling of the line profiles is difficult due to the relatively low S/Ns and poor velocity resolutions, several implications about the physical and chemical structures of the 4A1 and 4A2 cores, including their similarities and differences, can be obtained based on the results of our hyperfine fits.

The derived excitation temperatures are significantly different between 4A1 and 4A2, i.e., the excitation temperature in 4A2 (~ 150 K) is higher than that in 4A1 (~ 100 K). This difference is also clearly indicated by the higher peak brightness temperature in 4A2 (Figure 4). Since the excitation is expected to be thermalized, i.e., satisfies the LTE condition, the excitation temperatures can be directly used as a proxy of kinetic temperature. A similar trend has already been suggested by De Simone et al. (2020): they detected the optically thick CH_3OH emission to estimate kinetic temperatures of 100 K and 160 K for 4A1 and 4A2, respectively. The emitting region sizes of CH_3OH in De Simone et al. (2020; $0''.20$ – $0''.30$) are similar to the NH_3 emitting region sizes derived in the present work, suggesting that both CH_3OH and NH_3 trace a region with similar temperatures (see also De Simone et al. 2022). This is reasonable given that the sublimation temperature of CH_3OH and NH_3 are expected to be similar (100–140 K depending on the gas densities and major composition of the ice; e.g., Furuya & Aikawa 2014; Hama & Watanabe 2013; Minissale et al. 2022). The lower temperature of 4A1 may reflect either the higher column density of the dust or lower stellar and accretion luminosities.

The difference in the $\text{NH}_2\text{D}/\text{NH}_3$ ratios between 4A1 and 4A2 may in fact reflect the difference in the temperature. As discussed in the previous subsections, ices on the grain surface are expected to consist of two layers: the bulk mantle, with

lower deuteration formed in the molecular cloud stage, and the surface component, with higher deuteration synthesized in the dense core stage (e.g., Furuya & Persson 2018; Furuya et al. 2016; Taquet et al. 2013). Thus, the higher $\text{NH}_2\text{D}/\text{NH}_3$ ratio with a lower temperature in 4A1 may indicate that only the NH_3 ices in the surface layer have sublimated.

6. Summary

We have observed NH_3 and NH_2D high-excitation transitions at $\sim 1''$ resolution toward the protobinary NGC1333 IRAS4A with the VLA to measure the $\text{NH}_2\text{D}/\text{NH}_3$ ratio in the warm gas around the protostars, where ammonia ices have sublimated. Our main findings are summarized as follows:

1. We have detected NH_3 (1,1) to (5,5) inversion transitions with S/N of $\gtrsim 10$ toward both of the sources, 4A1 and 4A2. We have also detected NH_2D $3_{1,3}$ – $3_{0,3}$ and $4_{1,4}$ – $4_{0,4}$ rotation transitions with S/N ~ 5 toward 4A1, while they have been marginally detected with S/N ~ 3 – 5 toward 4A2.
2. We have estimated the excitation temperature and column density of NH_3 and NH_2D , and $\text{NH}_2\text{D}/\text{NH}_3$ column density ratios from the spectral line fitting. We found high NH_3 and NH_2D column densities of $\sim 10^{17}$ – 10^{18} cm^{-2} with high excitation temperatures ($\gtrsim 100$ K) for both 4A1 and 4A2, indicating that the NH_3 and NH_2D lines originate from the inner warm regions. The $\text{NH}_2\text{D}/\text{NH}_3$ ratios are remarkably high, ~ 0.5 – 1 . The ratio is $\gtrsim 0.3$, even if we take into account the slightly higher NH_3 column density derived by De Simone et al. (2022).
3. The high $\text{NH}_2\text{D}/\text{NH}_3$ ratios indicate the efficient formation of ammonia ices in the prestellar core stage, which in turn suggests that the primary nitrogen reservoir in molecular clouds is atomic nitrogen rather than nitrogen-bearing molecules such as N_2 and NH_3 .
4. In IRAS4A1, the line widths of NH_2D are similar to that of the NH_3 (3,3) transition, but are narrower than those of NH_3 higher transitions. This may indicate a ring-like distribution of NH_2D . The ring-like distribution of NH_2D and very high $\text{NH}_2\text{D}/\text{NH}_3$ ratio could be due to sublimation of multilayered ice mantle. The highly deuterated NH_3 ice is formed in the outermost layer of the ice mantle in the late stage of prestellar core and is the first to be sublimated when the grains fall onto the central warm regions.
5. The obtained D/H ratios of ammonia ices have been compared with those of other major volatiles in the IRAS4A core and the comet 67P. The higher D/H ratios of ammonia than those of water and methanol in IRAS4A indicate that ammonia ices are formed in the later stage of the prestellar core phase, where the deuteration is particularly efficient. The higher $\text{NH}_2\text{D}/\text{NH}_3$ ratio in IRAS4A than that in the comet 67P may suggest chemical reprocessing during the accretion onto the protostellar disk and subsequent protoplanetary disk phase. An alternative explanation is sublimation of a highly deuterated layer of ice mantle in IRAS4A.

We thank the anonymous referee for their valuable comments. We also thank Gianni Cataldi, Satoshi Yamamoto, Nami Sakai, and Yoko Oya for fruitful discussions and comments on the manuscript. We also thank Olli Sipilä and

Table 6
Spectroscopic Data of NH₃ and NH₂D Used in Hyperfine Fits

Transition	F	ν_0 (GHz)	g_u	$\log_{10} A_{ul}$ (s ⁻¹)	r^a	δv^b (km s ⁻¹)
NH ₃ (3, 3)	2-3	23.8678062	20.0	-7.5449	0.0264	29.1753
	4-3	23.8684499	36.0	-7.794	0.0268	21.0909
	3-3	23.8701279	28.0	-6.6658	0.28	0.0163
	4-4	23.8701296	36.0	-6.6174	0.4024	-0.005
	2-2	23.8701303	20.0	-6.642	0.2112	-0.0138
	3-4	23.8718076	28.0	-7.6846	0.0268	-21.0796
	3-2	23.872452	28.0	-7.6908	0.0264	-29.1728
NH ₃ (4, 4)	3-4	24.1369314	14.0	-7.7529	0.0162	30.8605
	5-4	24.1374943	22.0	-7.9457	0.0163	23.8697
	4-4	24.139415	18.0	-6.5927	0.3007	0.0161
	5-5	24.139417	22.0	-6.5648	0.3919	-0.0087
	3-3	24.1394175	14.0	-6.5771	0.2424	-0.0149
	4-5	24.1413376	18.0	-7.8583	0.0163	-23.861
	4-3	24.1419011	18.0	-7.8617	0.0162	-30.8593
NH ₃ (5, 5)	4-5	24.5303911	18.0	-7.9088	0.0109	31.7426
	6-5	24.5308986	26.0	-8.0659	0.011	25.541
	5-5	24.532987	22.0	-6.5396	0.3113	0.0208
	6-6	24.5329892	26.0	-6.5211	0.384	-0.0061
	4-4	24.5329897	18.0	-6.529	0.261	-0.0122
	5-6	24.5350777	22.0	-7.9932	0.011	-25.5275
	5-4	24.5355856	22.0	-7.9957	0.0109	-31.734
NH ₂ D 3 _{1,3} -3 _{0,3}	2-3	18.805907	15.0	-8.3826	0.0265	31.5766
	4-3	18.80649	27.0	-8.6324	0.0268	22.2837
	2-2	18.807831	15.0	-7.4793	0.2116	0.9086
	2-2	18.807831	27.0	-7.4562	0.4018	0.9086
	3-3	18.8080466	21.0	-7.5037	0.2801	-2.528
	3-4	18.809385	21.0	-8.523	0.0268	-23.8618
	3-2	18.8099083	21.0	-8.5284	0.0265	-32.203
NH ₂ D 4 _{1,4} -4 _{0,4}	3-4	25.0216041	7.0	-8.2179	0.0162	26.2117
	5-4	25.0221167	11.0	-8.4117	0.0163	20.0706
	3-3	25.0237541	7.0	-7.0417	0.2431	0.4541
	5-5	25.0237746	11.0	-7.0314	0.3911	0.2085
	4-4	25.0238552	9.0	-7.0582	0.3008	-0.7572
	4-5	25.0255132	9.0	-8.3244	0.0163	-20.6205
	4-3	25.0260052	9.0	-8.3268	0.0162	-26.5148

Notes.

^a Relative strengths of hyperfine transitions. Normalized as the sum of r being 1.

^b Velocity offsets with respect to the inversion or rotation transitions listed in Table 1.

Shota Notsu for providing the spectroscopic data of NH₃ and a physical model of IRAS4A which were used for discussions, respectively. Y.Y. acknowledges support from IGPEES, WINGS Program, the University of Tokyo. K.F. acknowledges support from JSPS KAKENHI grant Nos. 20H05847, 21H01145, and 21K13967. Y.A. acknowledges support by NAOJ ALMA Scientific Research Grant code 2019-13B, Grant-in-Aid for Scientific Research (S) 18H05222, and Grant-in-Aid for Transformative Research Areas (A) grant Nos. 20H05844 and 20H05847. J.K.J. acknowledges support from the Independent Research Fund Denmark (grant No. DFF0135-00123B). The National Radio Astronomy Observatory is a facility of the National Science Foundation operated under cooperative agreement by Associated Universities, Inc.

Facility: VLA

Software: astropy (Astropy Collaboration et al. 2013, 2018), bettermoments (Teague & Foreman-Mackey 2018), astroquery (Ginsburg et al. 2019), LIME (Brinch & Hogerheijde 2010), emcee (Foreman-Mackey et al. 2013)

Appendix A Hyperfine Models for NH₃ and NH₂D

Here we describe details of the hyperfine models for the observed NH₃ and NH₂D transitions.

A.1. NH₃ Model

We follow the methodology described in Rosolowsky et al. (2008). Observed spectra in terms of brightness temperature $T_B(\nu)$ are modeled as

$$T_B(\nu) = f(J_\nu(T_{\text{ex}}) - J_\nu(T_{\text{bg}}))(1 - e^{-\tau(\nu)}), \quad (\text{A1})$$

where f is the beam filling factor as in Equation (1), T_{ex} is the excitation temperature, T_{bg} is the background temperature (i.e., a cosmic microwave background temperature of 2.73 K here), and $\tau(\nu)$ is the optical depth profile. For each transition of NH₃,

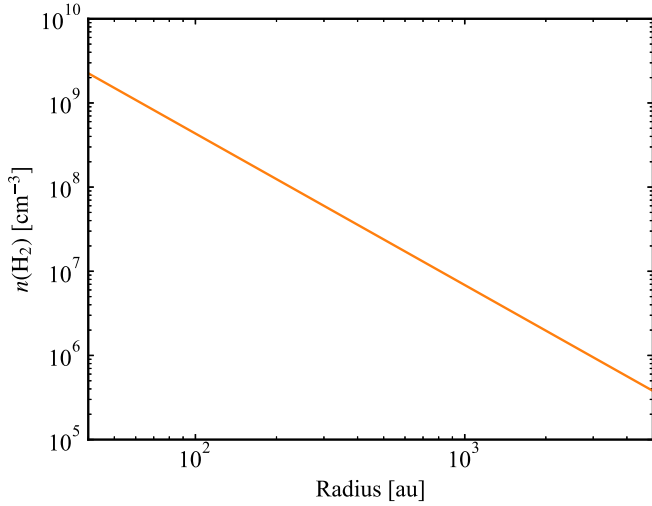


Figure 5. Gas density profile of the IRAS4A envelope presented in Persson et al. (2016).

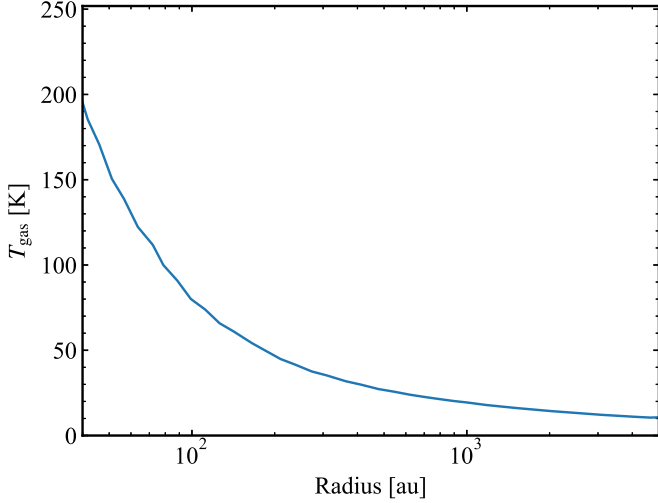


Figure 6. Dust temperature profile of the IRAS4A envelope presented in Persson et al. (2016).

$\tau(\nu)$ is given by

$$\tau(\nu) = \tau_0 \sum_i r_i \exp\left(-\frac{(\nu - \delta\nu_i - \nu_0)^2}{2\sigma_{v,i}^2}\right), \quad (\text{A2})$$

where τ_0 is the total optical depth of the transition, r_i , $\delta\nu_i$, and $\sigma_{v,i}$ are the relative strength, velocity offset, and line width of the i th hyperfine component, and ν_0 is the systemic velocity of the central protostar. The values of r_i , $\delta\nu_i$, and $\sigma_{v,i}$ are calculated as

$$r_i = \frac{g_{u,i} A_{ul,i}}{\sum_j g_{u,j} A_{u,j}}, \quad \delta\nu_i = \left(1 - \frac{\nu_i}{\nu_0}\right)c, \quad \sigma_{v,i} = \frac{\sigma_v}{c} \nu_i, \quad (\text{A3})$$

where ν_0 is the rest frequency of the inversion transition listed in Table 1, $g_{u,i}$, $A_{ul,i}$, and ν_i are the statistical weight, Einstein A coefficient for spontaneous emission, and the rest frequency of the i th hyperfine component, respectively (Table 6; Kukolich & Wofsy 1970; Kukolich 1967). These data are retrieved from the Cologne Database for Molecular Spectroscopy (CDMS; Müller et al. 2005) available at the Splatalogue database queried by

astroquery (Ginsburg et al. 2019). We assumed that the σ_v and ν_0 are common among the hyperfine components in the same inversion or rotational transition, given that they originate from the same temperature region.

The total optical depths of each transition are related back to the column density as in Friesen et al. (2009; see also Rosolowsky et al. 2008):

$$N(J, K) = \sqrt{2\pi} \sigma_v \frac{8\pi\nu_0^3}{c^3 A_{ul}} \frac{1 + \exp(-h\nu_0/k_B T_{\text{ex}})}{1 - \exp(-h\nu_0/k_B T_{\text{ex}})} \tau_0(J, K), \quad (\text{A4})$$

where $N(J, K)$ is the column density of NH_3 at the (J, K) metastable state. The column density $N(J, K)$ can be related with the total (ortho or para) NH_3 column density $N(\text{NH}_3)$ through the partition function Q as

$$N(\text{NH}_3) = \frac{Q(T_{\text{rot}})}{g_u} N(J, K) \exp\left(\frac{E_u}{T_{\text{rot}}}\right), \quad (\text{A5})$$

where g_u and E_u are the statistical weight and energy of the upper state listed in Table 1. The partition function Q is calculated following Wilson et al. (2009) as

$$Q(T) = \sum_{J=0}^{\infty} \sum_{K=0}^J (2J+1) S(J, K) \exp\left[-\frac{h(BJ(J+1) + (C-B)K^2)}{k_B T}\right], \quad (\text{A6})$$

where $B = 298117$ MHz and $C = 186726$ MHz are the rotational constants of NH_3 , and $S(J, K)$ is the constant factor for the nuclear spin statistics. For ortho- and para- NH_3 transitions, $S(J, K) = 4, 2$, respectively.

In the LTE approximation, the excitation temperature (T_{ex}) that governs the inversion transition and the rotational temperature (T_{rot}) that governs the population between the metastable levels are assumed to be the same, and these temperatures can be directly used as a proxy of the kinetic temperature (T_{kin}). In our fit, all of these temperatures are assumed to be the same and are represented by T_{ex} .

A.2. NH_2D Model

Our NH_2D model follows the same formulation as NH_3 . The spectroscopic data used for NH_2D are listed in Table 6 (Cohen & Pickett 1982; De Lucia & Helminger 1975; Fusina et al. 1988). Since we observed only a single transition for each ortho- and para- NH_2D , we directly related the optical depth to the column density assuming that T_{ex} is the same as that of NH_3 :

$$N_u = \sqrt{2\pi} \sigma_v \frac{8\pi\nu_0^3}{c^3 A_{ul}} \left[\exp\left(\frac{h\nu_0}{k_B T_{\text{ex}}}\right) - 1 \right] \tau_0, \quad (\text{A7})$$

where N_u is the NH_2D column density at the upper state of the transition. The total NH_2D column density is calculated as

$$N(\text{NH}_2\text{D}) = \frac{Q(T_{\text{ex}})}{g_u} N_u \exp\left(\frac{E_u}{T_{\text{ex}}}\right), \quad (\text{A8})$$

where Q is the full (i.e., ortho+para) partition function of NH_2D retrieved from the CDMS (Müller et al. 2005).

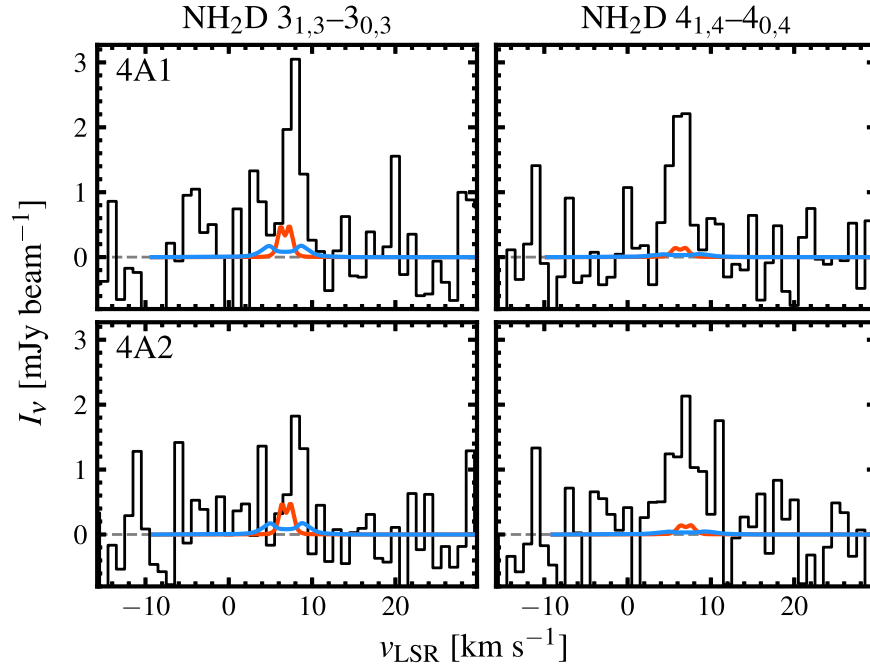


Figure 7. Comparison of model spectra of NH_2D transitions predicted by the non-LTE simulation with central stellar masses of $1.0 M_\odot$ (blue) and $0.08 M_\odot$ (orange) and observed spectra toward 4A1 (top) and 4A2 (bottom). The zero intensity level is indicated by the gray dashed line.

Appendix B Radiative Transfer Modeling

We simulated the spectra of NH_2D transitions using the non-LTE radiative transfer code LIME (Brinch & Hogerheijde 2010) to see if only the cold envelope component of NH_2D could reproduce the observed NH_2D emission. Here we will describe the simulation settings. As the density and temperature structures of the IRAS4A protostellar cores, we used the spherically symmetric envelope model presented in Persson et al. (2016). The gas density and dust temperature profiles are shown in Figures 5 and 6. The gas density follows a single power-law profile, $n = n_{\text{in}}(r/r_{\text{in}})^{-p_{\text{env}}}$, where the parameters $n_{\text{in}} = 3.1 \times 10^9 \text{ cm}^{-3}$, $r_{\text{in}} = 33.5 \text{ au}$, and $p_{\text{env}} = 1.8$ are constrained through simultaneous fits to submillimeter dust continuum radial profiles and spectral energy distributions (see also Jørgensen et al. 2002; Kristensen et al. 2012). For this profile of the gas density, the dust temperature profile is self-consistently calculated (Jørgensen et al. 2002; Kristensen et al. 2012; Persson et al. 2016) assuming the observed luminosity of $9.1 L_\odot$. We adopted this dust temperature profile as the gas temperature profile, i.e., assuming that the gas and dust are well coupled and their temperatures are the same. The modeled dust temperature inside the observed emitting region size ($\sim 75 \text{ au}$) is $\gtrsim 100 \text{ K}$, consistent with the observed excitation temperatures of ~ 100 and $\sim 160 \text{ K}$ (see Section 4). The radial profiles are truncated at r_{in} and $r_{\text{out}} = 33,500 \text{ au}$.

For the kinetics of the gas, we simply employed a spherically symmetric free-falling envelope with a radial velocity of $v_{\text{ff}} = \sqrt{2GM_*/r}$. We assumed a protostellar mass of $M_* = 1 M_\odot$ for both 4A1 and 4A2, given that there are almost no measurements of the central stellar mass. For 4A2, Choi et al. (2010) estimated it to be $0.08 M_\odot$ from the velocity gradient analysis of NH_3 emission. Thus, we took another run with $M_* = 0.08 M_\odot$ to evaluate the effect of the central stellar mass to the observed emission.

We calculated the NH_2D abundance in the cold envelope based on single-dish observations and the model H_2 column density. Hatchell (2003) observed the NH_2D rotation-inversion transition with the IRAM 30 m telescope (with a beam size of $\sim 25''$ or $\sim 7000 \text{ au}$), and derived an NH_2D column density of $3.9 \times 10^{14} \text{ cm}^{-2}$. This value is divided by the model H_2 column density of $1.9 \times 10^{24} \text{ cm}^{-2}$ (see Table C.1 in Kristensen et al. 2012), resulting in an NH_2D abundance of 2.1×10^{-10} . A constant abundance with radius is employed. The ortho-to-para ratio of NH_2D is fixed to 3, as done for the observational data analysis (Section 3).

The collisional excitation rates of ortho- NH_2D and para- NH_2D are based on Daniel et al. (2014) and taken from the Leiden Atomic and Molecular Database (Schöier et al. 2005). Given that the collisional excitation rates for ortho- H_2 and para- H_2 are available, we employ the thermal ortho-to-para ratio of H_2 (Flower & Watt 1984, 1985):

$$\frac{n(\text{ortho} - \text{H}_2)}{n(\text{para} - \text{H}_2)} = 9 \exp\left(-\frac{170.5 \text{ K}}{T}\right), \quad (\text{B1})$$

where T is the gas temperature. This ratio is low at low temperature, e.g., ~ 0.03 at 30 K .







We use the dust opacity with thin ice mantle presented in the fifth column of Table 1 in Ossenkopf & Henning (1994) and a standard gas-to-dust mass ratio of 100. The dust opacity is the same as the one used in the modeling by Persson et al. (2016).

We run the LIME code in its non-LTE mode to produce the model image cubes of the NH_2D $3_{1,3}-3_{0,3}$ and $4_{1,4}-4_{0,4}$ transitions. To simulate the observations, first we convolved the output image cubes by the 2D Gaussian with a FWHM of the beam major and minor axis. Then, we subtracted the continuum emission by the CASA task *imcontsub* and extracted the spectra toward the continuum peak by the same manner as the case of the observations.

The simulated spectra are compared to the observed spectra in Figure 7. The model with $0.08 M_\odot$ stellar mass shows the

brighter peak intensity due to the narrower line width caused by lower free-falling velocities. For both models, the peak intensities of the model spectra are weaker compared to the observed spectra by a factor of $\gtrsim 10$, except for $\text{NH}_2\text{D } 3_{1,3}-3_{0,3}$ with a central stellar mass of $0.08 M_\odot$. The cold component may partially contribute to $\text{NH}_2\text{D } 3_{1,3}-3_{0,3}$ emission ($\sim 20\%$ in velocity-integrated intensity) if the central stellar mass is small. We note, however, that the hyperfine splitting is not considered in this modeling. If it is considered, the peak intensity can be weaker because the total emission will be distributed over the hyperfine satellites. This is particularly effective for $\text{NH}_2\text{D } 3_{1,3}-3_{0,3}$, where it has a prominent splitting around the main component (see Table 6 for the hyperfine spectroscopic data). Thus, this comparison between model and observed spectra suggests that the observed emission cannot be reproduced by the cold component alone. Therefore, we suggest that the observed NH_2D emission indeed traces the NH_2D sublimated from ice in the hot corino rather than the cold envelope component, and the degree of NH_3 ice deuteration is indeed high in the protostellar cores of IRAS4A1 and 4A2. We emphasize that the purpose of the radiative transfer modeling presented here is to just evaluate the contributions of the cold component of NH_2D in the envelope to the observed emission. More detailed modeling is needed to reproduce the observed emission. Although the detailed physical structure on smaller scales can differ from the simple free-falling envelope model presented here (e.g., protostellar disk as considered by Choi et al. 2010), it is beyond the scope of the present work.

ORCID iDs

Yoshihide Yamato  <https://orcid.org/0000-0003-4099-6941>
 Kenji Furuya  <https://orcid.org/0000-0002-2026-8157>
 Yuri Aikawa  <https://orcid.org/0000-0003-3283-6884>
 Magnus V. Persson  <https://orcid.org/0000-0002-1100-5734>
 John J. Tobin  <https://orcid.org/0000-0002-6195-0152>
 Jes K. Jørgensen  <https://orcid.org/0000-0001-9133-8047>
 Mihkel Kama  <https://orcid.org/0000-0003-0065-7267>

References

- Aikawa, Y., Herbst, E., Roberts, H., & Caselli, P. 2005, *ApJ*, **620**, 330
 Aikawa, Y., Wakelam, V., Hersant, F., Garrod, R. T., & Herbst, E. 2012, *ApJ*, **760**, 40
 Altwegg, K., Balsiger, H., & Fuselier, S. A. 2019, *ARA&A*, **57**, 113
 Altwegg, K., Balsiger, H., Berthelier, J. J., et al. 2017, *RSPTA*, **375**, 20160253
 Altwegg, K., Balsiger, H., Hänni, N., et al. 2020, *NatAs*, **4**, 533
 Astropy Collaboration, Robitaille, T. P., Tollerud, E. J., et al. 2013, *A&A*, **558**, A33
 Astropy Collaboration, Price-Whelan, A. M., Sipőcz, B. M., et al. 2018, *AJ*, **156**, 123
 Bianchi, E., Codella, C., Ceccarelli, C., et al. 2019, *MNRAS*, **483**, 1850
 Boogert, A. C. A., Gerakines, P. A., & Whittet, D. C. B. 2015, *ARA&A*, **53**, 541
 Bottinelli, S., Boogert, A. C. A., Bouwman, J., et al. 2010, *ApJ*, **718**, 1100
 Brinch, C., & Hogerheijde, M. R. 2010, *A&A*, **523**, A25
 Caselli, P., Pineda, J. E., Sipilä, O., et al. 2022, *ApJ*, **929**, 13
 Choi, M., Kang, M., Tatematsu, K., Lee, J.-E., & Park, G. 2011, *PASJ*, **63**, 1281
 Choi, M., Tatematsu, K., & Kang, M. 2010, *ApJL*, **723**, L34
 Choi, M., Tatematsu, K., Park, G., & Kang, M. 2007, *ApJL*, **667**, L183
 Cohen, E. A., & Pickett, H. M. 1982, *JMoSp*, **93**, 83
 Daniel, F., Faure, A., Wiesenfeld, L., et al. 2014, *MNRAS*, **444**, 2544
 De Lucia, F. C., & Helminger, P. 1975, *JMoSp*, **54**, 200
 De Simone, M., Ceccarelli, C., Codella, C., et al. 2020, *ApJL*, **896**, L3
 De Simone, M., Ceccarelli, C., Codella, C., et al. 2022, *ApJL*, **935**, L14
 Di Francesco, J., Myers, P. C., Wilner, D. J., Ohashi, N., & Mardones, D. 2001, *ApJ*, **562**, 770
 Drozdovskaya, M. N., van Dishoeck, E. F., Rubin, M., Jørgensen, J. K., & Altwegg, K. 2019, *MNRAS*, **490**, 50
 Drozdovskaya, M. N., Schroeder, I. I. R. H. G., Rubin, M., et al. 2021, *MNRAS*, **500**, 4901
 Fedoseev, G., Ioppolo, S., Zhao, D., Lamberts, T., & Linnartz, H. 2015, *MNRAS*, **446**, 439
 Flower, D. R., & Watt, G. D. 1984, *MNRAS*, **209**, 25
 Flower, D. R., & Watt, G. D. 1985, *MNRAS*, **213**, 991
 Foreman-Mackey, D., Hogg, D. W., Lang, D., & Goodman, J. 2013, *PASP*, **125**, 306
 Friesen, R. K., Di Francesco, J., Shirley, Y. L., & Myers, P. C. 2009, *ApJ*, **697**, 1457
 Furuya, K., & Aikawa, Y. 2014, *ApJ*, **790**, 97
 Furuya, K., Drozdovskaya, M. N., Visser, R., et al. 2017, *A&A*, **599**, A40
 Furuya, K., & Persson, M. V. 2018, *MNRAS*, **476**, 4994
 Furuya, K., van Dishoeck, E. F., & Aikawa, Y. 2016, *A&A*, **586**, A127
 Furuya, K., Watanabe, Y., Sakai, T., Aikawa, Y., & Yamamoto, S. 2018, *A&A*, **615**, L16
 Fusina, L., Di Lonardo, G., Johns, J. W. C., & Halonen, L. 1988, *JMoSp*, **127**, 240
 Gibb, E. L., Whittet, D. C. B., Schutte, W. A., et al. 2000, *ApJ*, **536**, 347
 Ginsburg, A., Sipőcz, B. M., Brasseur, C. E., et al. 2019, *AJ*, **157**, 98
 Hama, T., & Watanabe, N. 2013, *ChRv*, **113**, 8783
 Hatchell, J. 2003, *A&A*, **403**, L25
 Hidaka, H., Watanabe, M., Kouchi, A., & Watanabe, N. 2011, *PCCP*, **13**, 15798
 Jensen, S. S., Jørgensen, J. K., Kristensen, L. E., et al. 2019, *A&A*, **631**, A25
 Jonusas, M., Leroux, K., & Krim, L. 2020, *JMoSt*, **1220**, 128736
 Jørgensen, J. K., Schöier, F. L., & van Dishoeck, E. F. 2002, *A&A*, **389**, 908
 Jørgensen, J. K., Müller, H. S. P., Calcutt, H., et al. 2018, *A&A*, **620**, A170
 Kristensen, L. E., van Dishoeck, E. F., Bergin, E. A., et al. 2012, *A&A*, **542**, A8
 Kukolich, S. G. 1967, *PhRv*, **156**, 83
 Kukolich, S. G., & Wofsy, S. C. 1970, *JChPh*, **52**, 5477
 Lacy, J. H., Faraji, H., Sandford, S. A., & Allamandola, L. J. 1998, *ApJL*, **501**, L105
 Lay, O. P., Carlstrom, J. E., & Hills, R. E. 1995, *ApJL*, **452**, L73
 Le Gal, R., Hily-Blant, P., Faure, A., et al. 2014, *A&A*, **562**, A83
 Loinard, L., Castets, A., Ceccarelli, C., Caux, E., & Tielens, A. G. G. M. 2001, *ApJL*, **552**, L163
 Looney, L. W., Mundy, L. G., & Welch, W. J. 2000, *ApJ*, **529**, 477
 Manigand, S., Jørgensen, J. K., Calcutt, H., et al. 2020, *A&A*, **635**, A48
 Maret, S., Bergin, E. A., & Lada, C. J. 2006, *Natur*, **442**, 425
 Martín-Doménech, R., Muñoz Caro, G. M., Bueno, J., & Goesmann, F. 2014, *A&A*, **564**, A8
 McMullin, J. P., Waters, B., Schiebel, D., Young, W., & Golap, K. 2007, in ASP Conf. Ser., 376, Astronomical Data Analysis Software and Systems XVI, ed. R. A. Shaw, F. Hill, & D. J. Bell (San Francisco, CA: ASP), 127
 Millar, T. J., Bennett, A., & Herbst, E. 1989, *ApJ*, **340**, 906
 Minissale, M., Aikawa, Y., Bergin, E., et al. 2022, *ESC*, **6**, 597
 Mottram, J. C., van Dishoeck, E. F., Schmalzl, M., et al. 2013, *A&A*, **558**, A126
 Müller, H. S. P., Schlöder, F., Stutzki, J., & Winnewisser, G. 2005, *JMoSt*, **742**, 215
 Nomura, H., & Millar, T. J. 2004, *A&A*, **414**, 409
 Notsu, S., van Dishoeck, E. F., Walsh, C., Bosman, A. D., & Nomura, H. 2021, *A&A*, **650**, A180
 Öberg, K. I., & Bergin, E. A. 2021, *PhR*, **893**, 1
 Öberg, K. I., Boogert, A. C. A., Pontoppidan, K. M., et al. 2011, *ApJ*, **740**, 109
 Ortiz-León, G. N., Loinard, L., Dzib, S. A., et al. 2018, *ApJ*, **865**, 73
 Ossenkopf, V., & Henning, T. 1994, *A&A*, **291**, 943
 Persson, M. V., Harsono, D., Tobin, J. J., et al. 2016, *A&A*, **590**, A33
 Persson, M. V., Jørgensen, J. K., van Dishoeck, E. F., & Harsono, D. 2014, *A&A*, **563**, A74
 Pickett, H. M., Poynter, R. L., Cohen, E. A., et al. 1998, *JQSRT*, **60**, 883
 Pineda, J. E., Harju, J., Caselli, P., et al. 2022, *AJ*, **163**, 294
 Przybilla, N., Nieva, M.-F., & Butler, K. 2008, *ApJL*, **688**, L103
 Rosolowsky, E. W., Pineda, J. E., Foster, J. B., et al. 2008, *ApJS*, **175**, 509
 Rubin, M., Altwegg, K., Balsiger, H., et al. 2015, *Sci*, **348**, 232
 Sahu, D., Liu, S.-Y., Su, Y.-N., et al. 2019, *ApJ*, **872**, 196
 Schöier, F. L., van der Tak, F. F. S., van Dishoeck, E. F., & Black, J. H. 2005, *A&A*, **432**, 369
 Schwarz, K. R., & Bergin, E. A. 2014, *ApJ*, **797**, 113
 Shah, R. Y., & Wootten, A. 2001, *ApJ*, **554**, 933
 Shirley, Y. L. 2015, *PASP*, **127**, 299
 Taquet, V., Chamley, S. B., & Sipilä, O. 2014, *ApJ*, **791**, 1

- Taquet, V., López-Sepulcre, A., Ceccarelli, C., et al. 2013, [ApJL](#), **768**, L29
- Taquet, V., Bianchi, E., Codella, C., et al. 2019, [A&A](#), **632**, A19
- Teague, R., & Foreman-Mackey, D. 2018, *RNAAS*, **2**, 173
- Tinacci, L., Germain, A., Pantaleone, S., et al. 2022, [ESC](#), **6**, 1514
- van der Tak, F. F. S., Schilke, P., Müller, H. S. P., et al. 2002, [A&A](#), **388**, L53
- van Dishoeck, E. F., Blake, G. A., Draine, B. T., & Lunine, J. I. 1993, in *Protostars and Planets III*, ed. E. H. Levy & J. I. Lunine (Tucson, AZ: Univ. Arizona Press), 163
- Wilson, T. L., Rohlfs, K., & Hüttemeister, S. 2009, *Tools of Radio Astronomy* (Berlin: Springer)
- Yu, S., Pearson, J. C., Drouin, B. J., et al. 2010, [JChPh](#), **133**, 174317
- Zucker, C., Speagle, J. S., Schlafly, E. F., et al. 2020, [A&A](#), **633**, A51